

# Effects of Macrosegregation and Microstructure on the Corrosion Resistance and Hardness of a Directionally Solidified Zn-5.0wt.%Mg Alloy

Talita Almeida Vida<sup>a</sup>, Thiago Soares<sup>a</sup>, Rudimylla Silva Septimio<sup>a</sup>, Crystopher Cardoso Brito<sup>b</sup> 

Noé Cheung<sup>a\*</sup> , Amauri Garcia<sup>a</sup>

<sup>a</sup> Departamento de Engenharia de Manufatura e Materiais, Universidade Estadual de Campinas - UNICAMP, Campinas, SP, Brasil

<sup>b</sup> Campus São João da Boa Vista, Universidade Estadual Paulista- UNESP, São João da Boa Vista, SP, Brasil

Received: January 07, 2019; Revised: June 09, 2019; Accepted: July 16, 2019

This study aims to analyze the influence of macrosegregation on microstructure evolution, and of microstructure length scale on the corrosion resistance of a Zn-5.0wt.%Mg alloy casting. The analyzed samples were taken along the length of castings unidirectionally solidified in unsteady state conditions of heat extraction. Microstructure characterization, microhardness, linear polarization and electrochemical impedance spectroscopy (EIS) tests were performed. A unique type of microstructure was observed, characterized essentially by a morphology typified by idiomorphic  $MgZn_2$  crystals in a “complex eutectic mixture” [coexistence of stable  $(Zn+Mg_2Zn_{11})$  and metastable  $(Zn+MgZn_2)$  eutectics]. The correlation between thermal and microstructural parameters, permitted experimental growth laws, correlating the evolution of the lamellar eutectic spacing with the cooling rate to be established. Vickers microhardness and electrochemical corrosion tests showed that more refined microstructures associated with higher experimental cooling rates, are related to a better set of higher hardness and corrosion resistance.

**Keywords:** Zn-Mg alloys, Solidification, Microstructure, Macrosegregation, Corrosion.

## 1. INTRODUCTION

Traditionally, Zn-Mg alloys are used as base alloys for steel coatings by galvanization. However, in recent years, studies have shown a nobler application for alloys of this system: the fabrication of biodegradable biomaterials for orthopedic applications <sup>1</sup>. Some Mg-based alloys have elasticity modulus similar to that of human bones, however, the corrosion rates associated with the release of hydrogen are conducive to increase in the degradation rate. In contrast, Zn-based alloys generally have lower corrosion rates in physiological solutions as compared to Mg-based alloys, which makes Zn-Mg alloys a good alternative as biodegradable biomaterials. Zn-Mg alloys, rich in Zn, have lower melting points and better machinability as compared to the same properties of Mg-based alloys <sup>1-3</sup>.

Vida et al. <sup>4</sup> analyzed hypoeutectic Zn-Mg alloys solidified under a transient regime of heat extraction and evidenced a columnar/equiaxed transition in alloys with Mg contents < 0.5wt.% (with columnar grains composed of a Zn matrix with a plate-like morphology and equiaxed Zn-rich dendritic grains). For alloys with Mg contents between 0.5 and 1.2wt.%, they observed only the growth of equiaxed grains of the Zn-rich dendritic matrix and a eutectic mixture in the interdendritic regions. Liu et al. <sup>5</sup> examined the microstructural behavior of Zn-Mg alloys having up to 4.5wt.% Mg solidified in a Bridgman device, using a range of solidification growth rates ( $v$ ) of 0.001-8 mm/s and a thermal gradient ( $G_1$ ) of 15 K/mm.

These authors reported six different microstructural morphologies with primary Zn dendrites and a variety of eutectic morphologies (rod, spherulitic and spiral). Nevertheless, studies on transient solidification conditions of hypereutectic Zn-Mg alloys for higher Mg concentrations, such as around 5%, and the resulting microstructure and properties have not yet been reported in literature, to the best of the authors knowledge and thus, is one of the aims of the present study.

The structural morphology of components produced through processes involving solidification may influence the corrosion resistance regarding the type of macro-morphological formation, e. g. columnar or equiaxed, or regarding determinant aspects of the microstructure. Generally, the mechanical strength increases with the decrease of most of the representative microstructural length scale, such as the dendritic arm spacings. However, this is not necessarily accompanied by the corrosion resistance, which strongly depends also on the electrochemical nature of the phases that compose the microstructure. This aspect demonstrates the influence of solute redistribution during solidification on the anodic or cathodic behavior of the phases of each alloy. In the case of eutectic systems, the volume fraction and morphology of the eutectic must be analyzed associated with dendritic spacings that may form localized micro-galvanic corrosion couples. The metallurgical evaluation of corrosion is not trivial, and requires a meticulous control of the evaluation criteria, which must consider not only the chemical composition of the alloy, but also the microstructure arrangement.

\*e-mail: [cheung@fem.unicamp.br](mailto:cheung@fem.unicamp.br)

In this sense, some authors have performed studies on electrochemical corrosion of as-solidified samples in order to correlate microstructure parameters with the resulting corrosion resistance<sup>1,4,6-9</sup>.

The electrochemical nature of corrosion phenomena has motivated the use of different evaluation techniques, such as the electrochemical impedance spectroscopy (EIS) and potentiodynamic polarization, based on measurements of electric properties of the system. In the EIS technique, an alternating current potential is applied to the system, in which the electric potential,  $E(t)$ , varies over time,  $t$ . The graphical representation provides a better viewing and analysis of the results. These graphs are called Nyquist, Bode and Bode phase diagrams. Through Nyquist diagrams, it is possible to represent the simulation of an equivalent electrical circuit (EC), which helps to interpret the results. Polarization is an important corrosion test that investigates a variety of electrochemical phenomena, which allows to study the reaction and kinetic mechanisms of corrosion and metal deposition phenomena. Potentiodynamic polarization is a method based on the measurement of the relation between potential and current density, through the excitation of continuous current signals. The Tafel extrapolation method is applied to polarization curves to establish values of corrosion potential ( $E_{\text{corr}}$ ), of thermodynamic nature, and kinetic current density ( $i_{\text{corr}}$ )<sup>10</sup>.

A recent study<sup>6</sup> investigated the corrosion behavior of two dilute Zn-Mg alloys: Zn-0.3wt.% Mg and Zn-0.5wt.% Mg. These alloys were unidirectionally solidified under a range of cooling rates, which permitted different microstructural morphologies to be formed (cellular and dendritic). The distinct microstructural characteristics of each alloy were correlated with the corrosion properties, obtained from electrochemical techniques (EIS and potentiodynamic polarization) in a 0.06M NaCl solution. The authors observed that, for both alloys, coarser microstructures showed higher corrosion rates as compared to refined microstructures. In another study<sup>7</sup>, the same methodology was used with Zn-1.2wt.%Mg and Zn-2.0wt.%Mg alloys. The increase in the alloy Mg content (from 1.2wt.% to 2.0wt.%) refined both the Zn-rich dendritic matrix and the lamellar eutectic mixture and reduced the volume fraction of the Zn-rich phase. The Zn-1.2wt.%Mg alloy has a lower eutectic fraction and a larger Ac/Aa ratio (relation between cathode and anode areas) as compared to that of the Zn-2.0wt.%Mg alloy and, consequently, the former alloy showed a greater resistance to corrosion. The EIS parameters demonstrated that the increase in the alloy Mg content is associated with the susceptibility to pitting corrosion, which induced greater corrosion action during tests with Zn-2.0wt.%Mg alloy samples.

Krieg et al.<sup>8</sup> characterized the microstructures of Zn-Mg alloys (1 to 3wt.%) solidified in a permanent mold and analyzed their corrosion behavior. The authors demonstrated that the corrosion action occurred in three stages:

surface activation, active corrosion and passivation by corrosion products, and emphasized that, in alloys with low Mg content, the microstructure did not affect the three stages, but only the stage of passivation was influenced by a more refined microstructure. In this sense, the authors concluded that the examined variation in the alloy Mg content does not lead to increase in the corrosion kinetics of Zn-Mg alloys, but rather the fineness of the microstructural arrangement was shown to be the main factor associated with it. Yao et al.<sup>9</sup> analyzed Zn-Mg alloys with different Mg contents and observed that an alloy containing 3wt.% Mg was more resistant to corrosion due to the formation of a nanostructured microstructure. Electrochemical tests performed in a 0.5M NaCl solution indicated a more positive corrosion potential for the Zn-3.0wt.%Mg alloy as compared to that of pure Zn, and a corrosion rate 34% higher for pure Zn. In this sense, the influence of the Mg content by itself on the corrosion behavior is still a controversial issue in literature. Based on the phase diagram of the Mg-Zn system,  $Zn_{11}Mg_2$  and Zn-rich are phases expected to occur only for a range of alloys having hypoeutectic to hypereutectic (~6wt.%Mg) concentrations, despite the dependences of morphology, scale and arrangement of the phases on the solidification conditions. The combined effect of the aforementioned microstructural features with the alloy Mg content on the corrosion response seems to be a more appropriate analysis path, which is expected to constitute another contribution of this work for Zn-Mg alloys having higher Mg content (5wt.%Mg).

Entering into a more specific analysis on the influence of the microstructural phases in the corrosion behavior, Prosek et al.<sup>11</sup> confirmed that the superior corrosion properties of Zn-Mg alloys are related to the presences of  $Mg_2Zn_{11}$  and  $MgZn_2$  intermetallic (IMC) phases. The available data indicated that the first IMC provided a better stability to corrosion. The phases were shown to be covered by a Mg-based oxide film formed at the initial stages of corrosion. The authors proposed that the formation of this film was the main reason for the reduction in the corrosion rate of Zn-Mg alloys. Byun et al.<sup>12</sup> also studied the corrosion resistance of these IMCs via potentiodynamic polarization followed by surface analysis. A dependency was observed between the Mg content of the alloy and the corrosion resistance. In addition, the authors highlighted that the  $Mg_2Zn_{11}$  IMC showed better corrosion resistance, which was attributed to the formation of intermediate products of corrosion, which were formed on the sample surface, thus preventing the direct exposition to the electrolyte. Among the oxidation products, the  $Zn_3(OH)_8Cl_2H_2O$  compound (simonkolleite) stands out, which contributed to delay the formation of ZnO, promoting better corrosion resistance. On the other hand, the improvement in corrosion resistance is not always the aim of Zn-Mg based alloys.

The literature shows that they are used when controlled degradation is required for specific applications, such as for the production of stents<sup>13</sup> and bone implants<sup>14</sup>.

The role of the cooling rate imposed during solidification on the morphology and scale of the phases forming an alloy microstructure is well known<sup>15-17</sup>, and these microstructural characteristics were shown to play important roles on the mechanical and corrosion properties of alloys<sup>18-21</sup>. As aforementioned, some studies reported in literature described the corrosion performance of Zn-Mg alloys, concerning the role of the alloy Mg content and also of microstructure<sup>8,9,11</sup>. However, there is still a lack of more comprehensive studies on correlations between microstructural parameters (phases morphology; length scale of the microstructural phases; phase fraction, etc.) and mechanical and corrosion behavior of Zn-Mg hypereutectic alloys, in particular for transient solidification conditions and under a wide range of cooling rates, which are typical of casting and galvanizing processes.

Therefore, this study initially aims to establish correlations between experimental thermal parameters during transient water-cooled unidirectional solidification of a Zn-5.0wt.%Mg alloy casting [growth rate ( $V_L$ ) and thermal gradient ( $G_L$ ) synthesized by the cooling rate ( $\dot{T}=G_L \cdot V_L$ )] and a representative microstructural parameter, that is, the interlamellar eutectic spacing ( $\lambda_{cut}$ ). The solidification technique to be used provides a wide range of cooling rates (and consequently of  $\lambda_{cut}$  values) along the length of the casting. This will permit also to assess the effects of  $\lambda_{cut}$  on Vickers microhardness and corrosion resistance along the entire length of the unidirectionally solidified casting.

## 2. Experimental Procedure

### 2.1 Materials

Commercially pure Zn and Mg (compositions shown in Table 1) were used to prepare the Zn-5.0wt.%Mg alloy. A vertical unidirectional water-cooled solidification setup was used to produce a directionally solidified (DS) Zn-5.0wt.%Mg alloy casting. A cylindrical mold was used, made of AISI 301 stainless steel, with internal diameter of 55mm, height of 150 mm, having a 5 mm thick disk of AISI 1020 carbon steel at the mold bottom, used to separate the casting from the cooling water. The mold has eight 1.6mm- diameter holes along its length for fixing the thermocouples used to monitor the evolution of temperatures in the DS casting. The molten alloy was poured into the cylindrical cavity of the mold and remelted by a set of electrical windings positioned externally along the length of the cylindrical mold.

When the desired superheat was achieved, the electrical windings were switched off and water flow was initiated, reaching the bottom of the mold, promoting directional heat extraction until the completion of solidification. More details regarding the used experimental setup can be found in previous studies<sup>4, 20, 22</sup>.

### 2.2 Characterization of Macro and Microstructure and Macrosegregation Profile

The DS casting was longitudinally sectioned, subsequently ground and etched with the Aqua Regia reagent (solution of 1:3 of nitric acid and hydrochloric acid, in volume) to obtain the macrostructure.

The cross-section samples for microstructure analysis were extracted along the length of DS casting, from the cooled bottom to the top. The microstructures were revealed by etching with 10% Nital reagent (10% nitric acid in ethyl alcohol) for 7 seconds. The images were acquired using an OLYMPUS GX41 microscope along with the OLYMPUS Stream Essentials® 1.9 software. The microstructural analysis was complemented by the use of a Carl ZEISS EVO MA 15 scanning electron microscope (SEM), equipped with an OXFORD energy-dispersive spectrometer (EDS), model X-MAX. The lamellar spacings of the eutectic mixture was measured with the aid of the Image-J software. For each sample at least 50 measurements were performed.

The samples used for segregation analyses were extracted from different cross-section positions along the length of the DS casting. Such analyses were carried out by X-ray fluorescence (XRF), using a spectrometer model Rigaku RIX-3100, through an area of 100 mm<sup>2</sup> probe.

### 2.3 Characterization of microstructural phases

The phases that constitute the microstructure of the Zn-5.0wt.%Mg alloy were determined through X-ray diffraction (XRD), in two samples associated with cooling rates that allowed obtaining both refined and coarse microstructures. The spectra were obtained through a diffractometer (model X'Pert PRO MRD XL, Panalytical), with scanning range of  $20^\circ \leq 2\theta \leq 90^\circ$ , X-ray tube of Cu - K $\alpha$  target and radiation of wavelength  $\lambda = 1.5405 \text{ \AA}$ .

### 2.4 Mechanical test: Microhardness

The Vickers microhardness was measured in the same samples used in the microstructural analysis. The tests were performed in a Shimadzu HMV microdurometer, with 0.5 kgf load and for a dwell time of 15 s. The adopted hardness value of a representative position in the DS casting was the average of at least 20 measurements on each sample.

**Table 1.** Chemical composition of commercially pure Zn and Mg (wt.%)

Element	Zn	Mg	Mn	Cr	Fe	Al	Pb	Si
Zn	Balance	-	-	-	0.015	-	0.012	0.003
Mg	0.01	Balance	0.01	0.01	0.01	0.11	-	-

## 2.5 Electrochemical Tests

The tests of electrochemical impedance spectroscopy (EIS) and potentiodynamic polarization were performed in samples ground and polished through 1  $\mu\text{m}$  diamond paste finish and subjected to ultrasonic cleaning. The electrochemical tests were performed in samples extracted from regions of the DS casting that were subjected to high and low cooling rates during solidification in order to analyze the influence of different microstructural arrangements on the corrosion behavior. The tests were carried out in triplicate in order to ensure reproducibility of the results. Before the beginning of each test, the samples were washed with distilled water and dried to eliminate any dirt on the area to be tested. Corrosion tests were conducted using a potentiostat/galvanostat model PGSTAT 128N by Autolab, and the NOVA 1.1 software. The electrochemical cell was composed of a working electrode (alloy samples), platinum wire used as counter-electrode, a silver/silver chloride (Ag/AgCl) reference electrode, and an electrolyte consisting of a 0.06 M NaCl solution at room temperature (25°C). To minimize electromagnetic effects from the environment, the electrochemical cell was mounted inside a Faraday cage.

Impedance tests were conducted in a frequency range from 100kHz to 100mHz and amplitude adjusted to 10mV regarding the open circuit potential. Before the impedance tests, the samples were subjected to measurements of the open circuit potential (OCP) for 900 seconds, enough to reach their stationary states. In all tests, an area of 0.503  $\text{cm}^2$  was used, corresponding to a circle area with diameter of 8mm. The EIS tests results are Bode, Bode-phase and Nyquist curves. In order to provide a support to discuss the experimental EIS results, a model was proposed in NOVA 1.1 software involving the fitting based on the complex non-linear least square (CNLS)<sup>23</sup>, to quantify the equivalent circuit (EC).

The polarization tests were performed at a scan rate of 0.16 mV/s from -100mV (ag/AgCl) to +250mV (Ag/AgCl) with respect to OCP. The polarization curves were expressed as a function of the current density and electrode potential, with a view to determining the corrosion current density ( $i_{\text{Corr}}$ ) and the corrosion potential ( $E_{\text{Corr}}$ ) through the Tafel's extrapolation method.

## 3. Results and Discussion

### 3.1 Cooling curves, cooling rates and macrosegregation profile

The Zn-5.0wt.%Mg alloy investigated in this study, is indicated by a vertical line in the Zn-Mg partial phase diagram of Figure 1, calculated by the Thermo-Calc software.

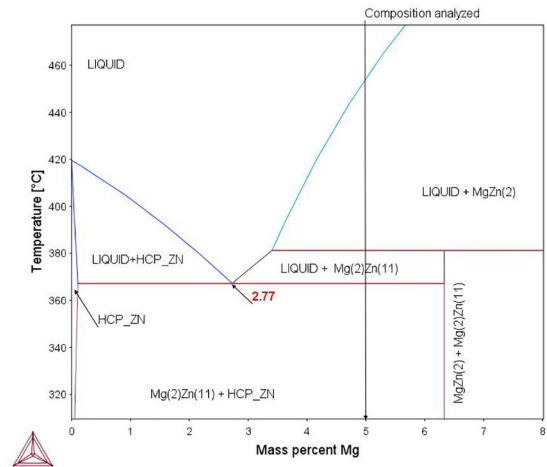


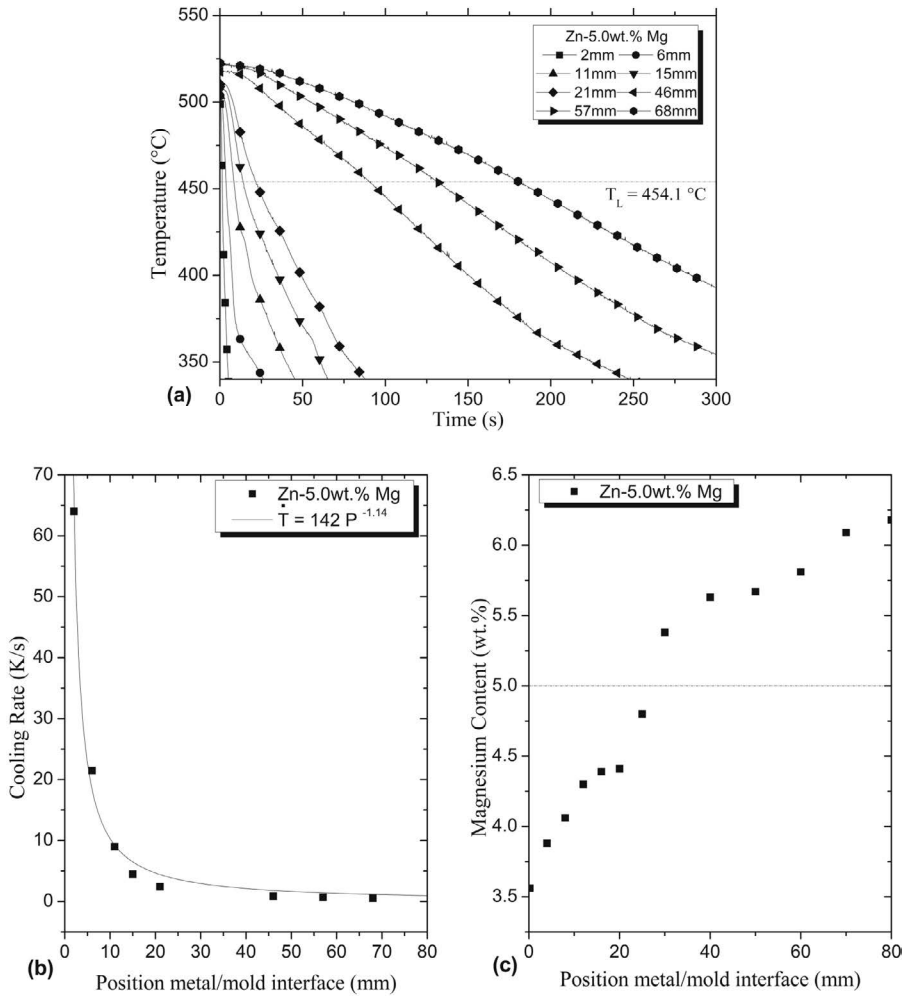
**Figure 1.** Zn-Mg partial phase diagram with indications of the analyzed alloy. Thermo-Calc PBIN database.

The cooling curves [Figure 2(a)] were acquired from temperatures recorded by eight K-type thermocouples positioned along the center line of the DS casting at different positions, from the cooled bottom. The cooling rates ( $\dot{T} = dT/dt$ ), shown in Figure 2(b), were obtained by deriving the experimental thermal profiles with respect to time, immediately after the passage of the *liquidus* isotherm by each thermocouple<sup>4,20</sup>. Figure 2(c) shows the results of Mg macrosegregation along the length of the DS casting, obtained by XRF, where a normal macrosegregation profile can be observed. Mg is rejected into the liquid at the solidification front, thus providing a Mg-rich liquid just ahead this interface. Since Mg is much less dense than Zn, this Mg-rich liquid tends to move upwards, promoting consequently an increasing Mg profile from the bottom to the top of the vertical DS casting, as shown in Figure 2(c).

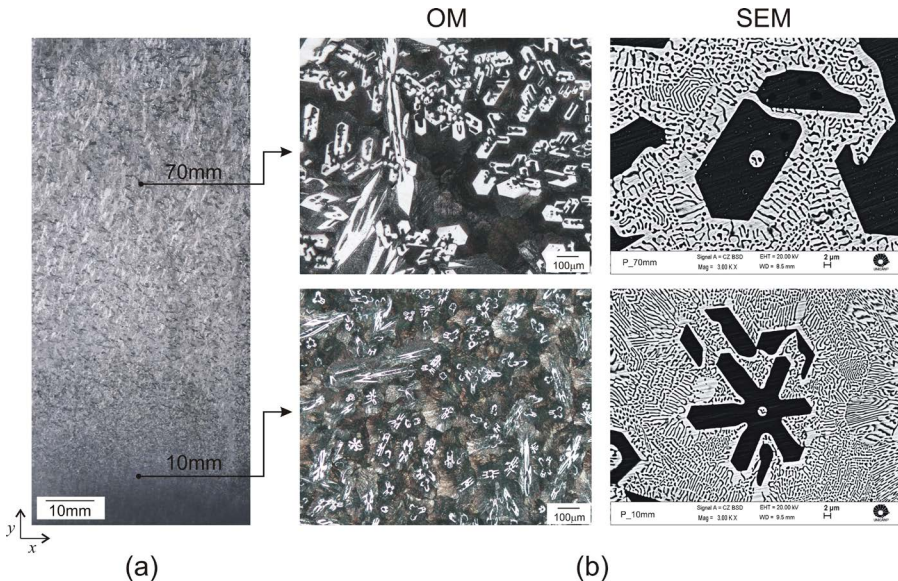
### 3.2 Characterization of the Macro and Microstructure

Figure 3 shows the macrostructure of the DS casting and the typical microstructures of samples from positions 10mm and 70mm, from the cooled bottom, i.e. solidified under cooling rates of  $\dot{T} = 10.3$  K/s and  $\dot{T} = 1.1$  K/s, respectively. The macrostructure consists essentially of equiaxed grains along the entire casting. The microstructures are essentially formed by eutectic mixtures and an idiomorphic phase (Figure 3b). A similar morphology was reported in studies by Prosek et al.<sup>11</sup> and Yao et al.<sup>24</sup>. With the increase in the distance from the cooled bottom of the casting, the microstructure coarsens due to the decrease in the cooling rate, which is reflected into both the eutectic and intermetallic lamellae, as shown in Figure 3b.

Figure 4 shows the X-ray diffractograms for the samples of both examined positions — 10 and 70 mm, representing regions of high and low cooling rates, respectively, as shown in Figure 3(b). A Zn-rich eutectic matrix characterizes the microstructure along the entire length of the DS casting.



**Figure 2.** (a) Experimental cooling curves; The numbers in the label, represent the position of the thermocouples (P) from the cooled bottom of the casting (P=0); (b) Cooling rate as a function of (P); (c) Mg concentration profile along the length of the vertical DS casting.



**Figure 3.** (a) Macrostructure and (b) Microstructure in optical microscope (OM) and scanning electron microscope (SEM) for positions: P\_10mm and P\_70mm, in which P is the distance from the cooling bottom.

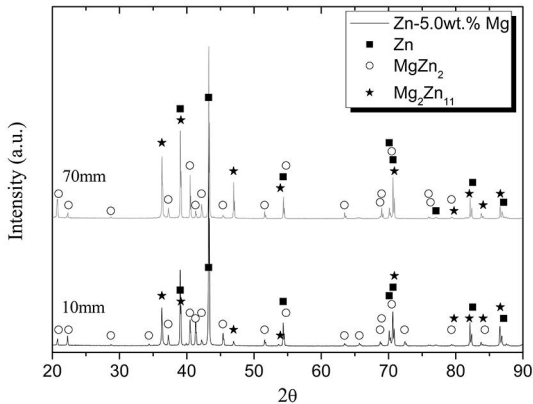
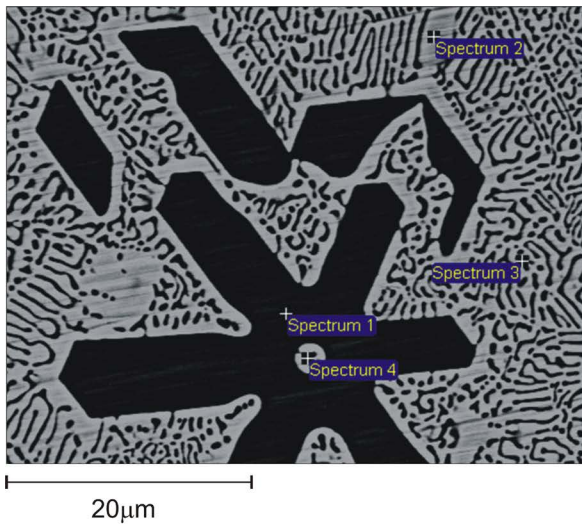


**Figure 4.** Patterns of X-ray diffraction.

Both the  $MgZn_2$  (or  $Zn_2Mg$ ) and  $Mg_2Zn_{11}$  (or  $Zn_{11}Mg_2$ ) IMCs were identified in the Zn-rich eutectic mixture.

The Zn-Mg system is known for featuring two competitive types of eutectic mixture<sup>5</sup>,  $Zn+Mg_2Zn_{11}$  and  $Zn+MgZn_2$ . Although diffractograms referring to only two positions in the casting are being shown in Figure 4, these two types of eutectics were observed along the entire length of the DS casting. The Zn-5.0wt.%Mg alloy is a hypereutectic composition of the Zn-Mg system, thus the  $MgZn_2$  phase composes the primary phase predicted by the phase diagram of Figure 1 and it was detected for the entire range of analyzed cooling rates. The determination of these IMCs will be important to the understanding of their influence on microhardness and corrosion behavior.

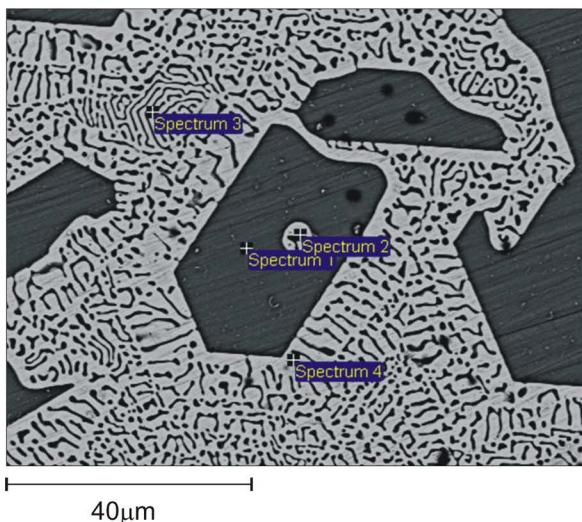
In addition to XRD, SEM/EDS analyses were performed, as shown in Figure 5, which allowed to quantitatively obtain the content of each element of the phases forming the microstructure of the alloy. Next to each image, a table is shown with the specific results of the analysis in weight wt.% and atomic at. % of Mg.



P\_10 mm

Spectrum	Mg	
	wt.%	at.%
Spectrum 1	15.2	32.5
Spectrum 2	0.2	0.5
Spectrum 3	3.1	7.9
Spectrum 4	8.6	20.2

(a)



P\_70 mm

Spectrum	Mg	
	wt.%	at.%
Spectrum 1	15.9	38.9
Spectrum 2	1.3	3.1
Spectrum 3	2.4	5.8
Spectrum 4	0.7	1.7

(b)

**Figure 5.** SEM micrographs of the Zn-5wt.%Mg alloy at (a) P\_10mm and (b) P\_70mm. Points 1, 2, 3 and 4 indicate local wt.% concentration of Zn/Mg obtained by SEM-EDS microprobe analyses. P is the position from the cooled bottom of the casting.

It was observed that the Zn-Mg alloy exhibited two competitive types of eutectic mixture [coexistence of stable eutectic ( $\text{Zn}+\text{Mg}_2\text{Zn}_{11}$ ) and metastable eutectic ( $\text{Zn}+\text{MgZn}_2$ )], plus idiomorphic crystals of the  $\text{MgZn}_2$  IMC. In Figure 5, the EDS analysis of Point 1 defined the  $\text{MgZn}_2$  idiomorphic phase (highest Mg content). The lighter region represented by Point 2 [Figure 5(a)] and Point 4 [Figure 5(b)] indicates the Zn-rich phase of the eutectic mixture, and the darker region indicated by Points 3 and 4 [Figure 5(a)] and Points 2 and 3 [Figure 5(b)] shows different values of Mg content within the eutectic region. This indicates the simultaneous occurrence of stable and metastable eutectics, and regions with contents of up to 6.3wt.%Mg corresponding to the stable eutectic mixture ( $\text{Zn}+\text{Mg}_2\text{Zn}_{11}$ ). Regions with contents above 6.3wt.%Mg correspond to the metastable eutectic ( $\text{Zn}+\text{MgZn}_2$ ), where the incidence of stable eutectic can also occur. It is worth mentioning that the SEM/EDS analysis may show a certain discrepancy regarding the measurement of slender phases, especially with thicknesses smaller than that of the EDS beam (the X-ray beam of the used equipment has a diameter of approximately  $1\mu\text{m}$ ).

Figure 6 graphically represents the evolution of the eutectic interphase spacing ( $\lambda_{\text{cut}}$  - interlamellar spacing) as a function of the solidification cooling rate ( $\dot{T}$ ). It can be observed that the experimental  $\lambda_{\text{cut}}$  values were fitted by a power function, with a  $-1/4$  exponent. This value agrees with that of the classical Jackson-Hunt equation for the growth of lamellar eutectics<sup>25</sup>. This experimental growth law agrees with that previously determined in a recent study with hypoeutectic Zn-Mg alloys<sup>4</sup>.

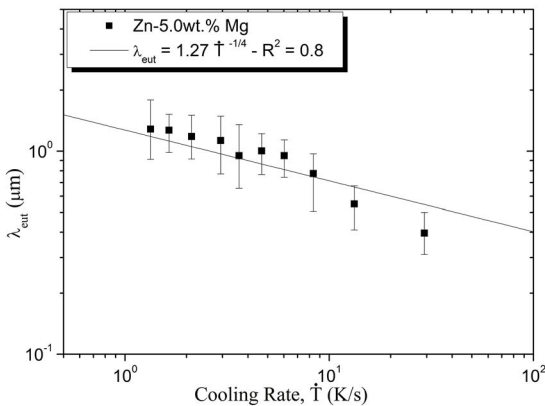


**Figure 6.** Evolution of the eutectic interphase spacing ( $\lambda_{\text{cut}}$ ) as a function of the solidification cooling rate ( $\dot{T}$ ).

### 3.3 Microhardness

The microhardness tests were performed in transversal samples extracted along the entire length of the DS casting. The objective was to understand the interaction between the lamellar matrix and the  $\text{MgZn}_2$  phase ( $\text{HV}_{\text{MgZn}_2} = 330$ <sup>26</sup>), considering the role of macrosegregation, and the corresponding effect on the experimental microhardness profile.

Figure 7 shows the experimentally measured values of Vickers microhardness as a function of both the eutectic interphase spacing ( $\lambda_{\text{cut}}$ ) and the solidification cooling rate ( $\dot{T}$ ). It can be seen a slight increase in microhardness (of about 115 to 130  $\text{HV}_{0.5}$ ) with the decrease in  $\lambda_{\text{cut}}$  (increase in  $\lambda_{\text{cut}}^{-0.5}$ ). The growing Mg profile from bottom to top of the DS casting [Figure 2(c)] combined with the reduction in the solidification cooling rate towards the top of the casting affect the size and volume fraction of  $\text{MgZn}_2$  particles. Higher cooling rates generate a more refined eutectic morphology, which associated with a more uniform distribution of fine idiomorphic  $\text{MgZn}_2$  crystals in the eutectic matrix [see Figure 3(b)], induced a better microhardness response.

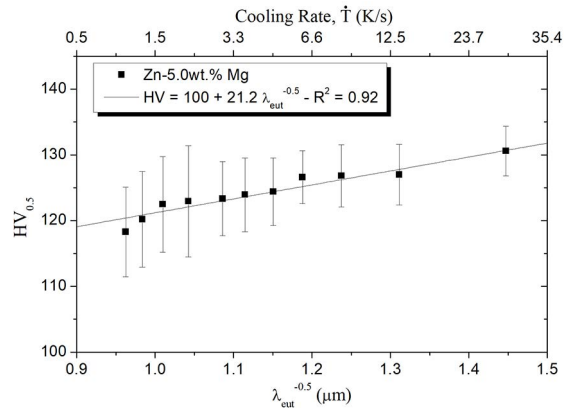


**Figure 7.** Vickers microhardness profile ( $\text{HV}_{0.5}$ ) as a function of the eutectic interphase spacing ( $\lambda_{\text{cut}}$ ) and cooling rate ( $\dot{T}$ ).

### 3.4 Electrochemical tests

#### 3.4.1 Electrochemical Impedance Spectroscopy (EIS) and Equivalent Circuit (EC)

The corrosion tests were performed in samples extracted from quite different positions along the length of the DS casting with a view to correlating the corrosion behavior of microstructures solidified under quite different solidification cooling rates ( $\dot{T}$ ).

The results of Electrochemical Impedance Spectroscopy (EIS) tests, experimental and simulated by the (CNLS) for samples (P\_10mm and P\_70mm), are plotted in Figure 8. Each sample has a different microstructure, refined and coarse, respectively, as shown in Figure 3. The Nyquist diagram [Figure 8(a)] showed two poorly defined capacitive semicircles (high and low frequencies) and an inductive process (low frequency) for both samples. The semicircles have wider diameters for P\_10mm, reflecting a slower electrochemical process<sup>27</sup>, which indicates a better resistance to corrosion or the formation of a protective layer. A qualitative analysis of the Nyquist diagrams allows to infer that the sample P\_10mm has a better corrosion behavior as compared to that of sample P\_70mm. Figure 8(b) shows the Bode and Bode-phase diagrams of the same two samples.

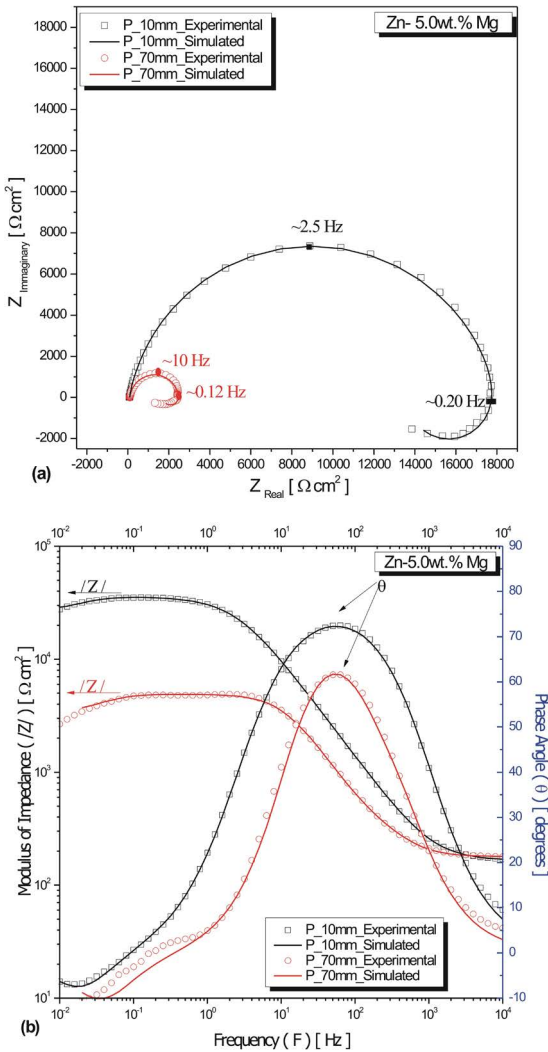


**Figure 8.** Comparison of the experimental and simulated CNLS results for the Zn-5.0wt.%Mg alloy samples P\_10mm and P\_70mm: (a) Nyquist graphs; High frequencies values indicated at the semicircles are related to the maximum imaginary component; while low frequencies values are related to the start of the inductive behavior. (b) Bode and Bode-phase graphs; The arrows indicate the maximum angle ( $\theta$ ) and the impedance module ( $|Z|$ ) values.

The impedance module increases with the decrease in frequency. For lower frequencies,  $|Z| = \sim 28 \text{ k}\Omega \text{ cm}^2$  for P\_10mm and  $|Z| = \sim 2.7 \text{ k}\Omega \text{ cm}^2$  for position 70mm can be observed. The higher  $|Z|$  values of sample P\_10mm suggest better behavior against corrosion. A similar behavior can be observed in the Bode-phase diagram, with the sample P\_10mm showing a maximum phase angle ( $\theta$ ) of  $\sim 72^\circ$  at 63 Hz, while sample P\_70mm exhibits a value ( $\theta$ ) of  $\sim 61^\circ$  at 50 Hz. From these comparative and qualitative observations, a better resistance to electrochemical corrosion is shown to be associated with sample P\_10mm.

This indicates that this trend can be directly associated with both the fineness of the microstructure (the position closest to the cooled bottom of the casting, 10mm, corresponds to a more refined microstructure), and Mg macrosegregation (lower Mg content of  $\sim 4.2\%$  for P\_10mm, and higher of  $\sim 6.1\%$  for P\_70mm), as shown in Figure 2(c).

The deviations of the impedance measurements described at the high frequency range ( $> 1 \text{ E}4 \text{ Hz}$ ) have been extensively discussed in the literature for different metal/electrolyte systems. In general, this type of dispersion is related to the influence of the impedance of the electrical conductors (connections between the sample and the measuring equipment) as well as to the intrinsic inductance of the system being studied<sup>28</sup>. In principle, these arcs or parasitic loops at high frequencies were mainly described in low conductivity electrolytes. The removal of these artifacts by a suitable selection of the geometry and design of the electrochemical cell is always desirable. However, it is worthwhile to highlight that their presence does not invalidate the impedance measurement, but limits the maximum frequency range from which the spectra may be analyzed.

In order to quantify the impedance parameters, an equivalent circuit is used to evaluate the corrosion mechanism that may be occurring in a short immersion time (15 min), thus allowing a more consistent correlation with microstructure and macrosegregation effects. An equivalent circuit (EC) is proposed  $[R_{el}(CPE_{(1)}[R_{(1)}(CPE_{(2)}R_{(2)}[L_{(1)}R_{(L)}]])]$ , as shown in Figure 9. The values attributed for each one of the EC elements and chi-squared values ( $\chi^2$ ) are shown in Table 2.

**Table 2.** Results of the simulated impedance parameters for the P\_10mm and P\_70mm of the Zn-5.0wt.%Mg alloy casting.

Parameters	Zn-5.0wt.%Mg	
	P_10mm	P_70mm
$R_{el} (\Omega \text{ cm}^2)$	83( $\pm 0.5$ )	90( $\pm 1.08$ )
$CPE_{(1)} (10^{-6} \text{ F/cm}^2)$	4.5( $\pm 0.17$ )	5.7( $\pm 0.17$ )
$R_1 (10^3 \Omega \text{ cm}^2)$	8.35( $\pm 0.24$ )	0.44( $\pm 0.07$ )
$n_1$	0.90	0.95
$CPE_{(2)} (10^{-6} \text{ F/cm}^2)$	3.62( $\pm 0.87$ )	2.5( $\pm 0.2$ )
$R_2 (10^3 \Omega \text{ cm}^2)$	9.8( $\pm 0.37$ )	1.94( $\pm 0.07$ )
$n_2$	0.54	0.96
$L (10^3 \text{ H cm}^2)$	150(fixed)	18.6(fixed)
$R_L (10^3 \Omega \text{ cm}^2)$	11.2( $\pm 1.0$ )	3.05( $\pm 0.44$ )
$\chi^2$	$9.3 \times 10^{-3}$	$82.7 \times 10^{-3}$

The use of this type of EC for different alloys can be found in the literature<sup>7,29-31</sup>. The EC adopted in this manuscript was presented and used in a recent work with Zn-Mg alloys<sup>7</sup>.

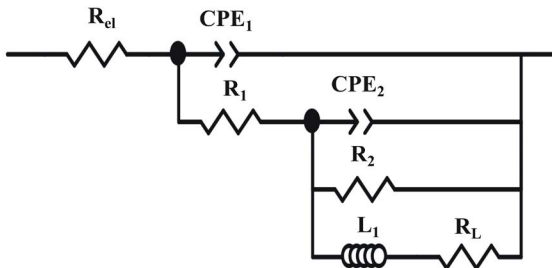


**Figure 9.** Schematic representation of the equivalent circuit (EC) used for P\_10mm and P\_70mm.

As they are binary alloys of the same system, there are no major modifications in the phases that will form the galvanic couples, only occurring increase in the fraction of a given phase, which shows that the used CE satisfies with reliability (with good  $\chi^2$ ) the study performed. The equivalent circuit adopted in this work was able to predict these three distinct time-constants, with a chi-square ( $\chi^2$ ) value of  $10^{-3}$ <sup>6,32-34</sup>, which makes the EC acceptable. An equivalent circuit with two time-constants was also analyzed by the authors, however, the experimental and simulated curves did not converge adequately and acceptably, providing  $\chi^2 > 10^{-1}$ .

The same equivalent circuit was adopted for the two samples (Figure 9) consisting of three time-constants, two associated with a capacitive semicircle (high and low frequencies) and one with an inductive process (low frequency) for both positions. In the EC used,  $R_{el}$  is the resistance of the electrolyte, that is, about  $83 \Omega\text{cm}^2$  and  $90 \Omega\text{cm}^2$  for P\_10mm and P\_70mm, respectively.  $R_1$  and  $R_2$  correspond to the resistances for charge transfer of the porous (outer) and barrier (inner) layers, respectively. Larger values of  $R_1$  and  $R_2$  for P\_10mm give indications of higher corrosion resistance. The capacitances, associated with the double layer and film layer, are represented by the constant phase elements,  $CPE_{(1)}$  and  $CPE_{(2)}$ , respectively. An inductor element and its corresponding resistance is also considered. Inductive arcs are attributed to adsorption and reduction of corrosion products at the interface between the electrolyte and the sample<sup>30, 35</sup>. The relaxation of species in the oxide layer due to adsorption and incorporation of  $\text{Cl}^-$  ions in the oxide film is also frequently considered<sup>36,37</sup>. The inductive arc might be associated with the beginning of pits formation<sup>38,39</sup>. In this study, the presence of  $\text{Zn}_2\text{Mg}$  and  $\text{Zn}_{11}\text{Mg}_2$ , determined by the X-Ray diffractograms of Figure 4, is responsible for the pitting corrosion, since they have anodic behavior as compared to that of the Zn matrix. Yao and coauthors<sup>1</sup> stated that  $-740 \text{ mV}$  (Standard Hydrogen Reference Electrode - SHE), and  $-790 \text{ mV}$  (SHE) are the corresponding potentials for Zn and  $\text{Mg}_2\text{Zn}_2$ , respectively. Additionally, Prosek and coauthors<sup>11</sup> stated that  $-1070 \text{ mV}$  (SHE) is the corresponding potential for  $\text{Mg}_2\text{Zn}_{11}$ . This evidences that the Zn-rich phase has a nobler potential with respect to Mg in the examined NaCl solution.

As shown by the impedance parameters of Table 2, the sample P\_70mm has a lower corrosion resistance as compared to that of P\_10mm. The porous resistances ( $R_1$ ) are smaller than the resistance of internal oxide layers ( $R_2$ ). With respect to  $CPE_{(2)}$  and  $R_2$ , it can be observed that  $CPE_{(2)}$  is of the same order of magnitude for both samples, while  $R_2$  indicates greater resistance to corrosion associated with the sample P\_10mm. When the inductor parameters are analyzed, the inductances (L) and the resistances ( $R_L$ ) are approximately  $150 \text{ kH.cm}^2$  and  $11.2 \text{ k}\Omega\text{.cm}^2$  (P\_10mm) and  $18.6 \text{ kH.cm}^2$  and  $3.0 \text{ k}\Omega\text{.cm}^2$  (P\_70mm), respectively, therefore, around 8 and 4 times greater for the sample P\_10mm as compared to the values of sample P\_70mm. This seems to indicate more intense pits formation (and deeper pits) with the higher Mg content of sample P\_70mm (coarser microstructure), since a smaller  $R_L$  indicates greater susceptibility to pitting corrosion. In this sense, EIS parameters indicate that the most refined microstructure (P\_10mm) shows a better electrochemical behavior than the coarser microstructure (P\_70mm), therefore, it is less susceptible to pitting corrosion.

### 3.4.2 Potentiodynamic polarization

From the polarization curves, by applying the Tafel extrapolation method, two important parameters that characterize the corrosion resistance: the corrosion potential ( $E_{\text{corr}}$ ) and the corrosion current density ( $i_{\text{corr}}$ ), can be determined according to the ASTM G102 standard. Figure 10 shows the typical experimental potentiodynamic polarization curves along a potential range between  $-1.1 \text{ V}$  and  $-0.7 \text{ V}$  (vs. Ag/AgCl), as well as the average experimental values of corrosion current density ( $i_{\text{corr}}$ ) and corrosion potential ( $E_{\text{corr}}$ ) for samples P\_10mm and P\_70mm. The ( $E_{\text{corr}}$ ) and ( $i_{\text{corr}}$ ) values are listed in Table 3.

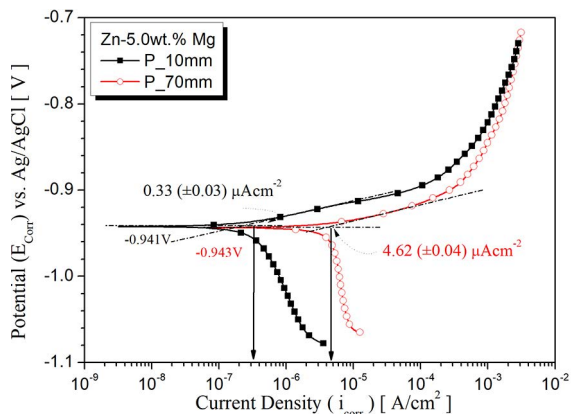


**Figure 10.** Potentiodynamic polarization curves of the Zn-5.0wt.%Mg alloy for samples of positions P\_10mm and P\_70mm.

**Table 3.** Polarization parameters for samples (P\_10mm) and (P\_70mm) of the Zn-5.0wt.%Mg alloy casting.

Parameters	Zn-5.0wt.%Mg	
	P_10mm	P_70mm
$E_{\text{corr}}$ (mV)	-941	-943
$i_{\text{corr}}$ ( $\mu\text{A.cm}^2$ )	0.33 ( $\pm 0.03$ )	4.62 ( $\pm 0.04$ )

The curves show that both samples presented an anodic branch under control by activation while the cathodic branch shows control by diffusion, characterized by a practically vertical cathodic branch<sup>7</sup>. It can be observed that, for the sample P\_70mm, the polarization curve shifted to the right, associated with greater current densities. In general, a same corrosion potential is related to both samples, however, the current density showed a difference of approximately one decade. In this sense, the lower corrosion rate of sample P\_10mm gives an indication of better behavior against corrosion as compared that of sample P\_70mm, as also indicated by the EIS parameters previously analyzed.

The different phases that constitute the Zn-5.0wt.%Mg alloy microstructure show a different corrosion behavior. Because the difference of potential between these phases, localized corrosion is generated, thus favoring the dissolution of the phase having the lower corrosion potential. Figure 11 shows images obtained by a scanning electron microscope of samples P\_10mm and P\_70mm after the corrosion tests. Figures 11 (a) and (c) show that the corrosion initiates in the intermetallic phase of the eutectic, and Figures 11 (b) and (d) show the most corroded eutectic region of both samples.

By comparing the corrosion attack morphologies of the two samples, for P\_10mm, a lower degradation aspect can be realized as compared to the one of P\_70mm, which justifies the lower chemical activity shown in the corrosion tests.

In the studied alloy, Zn-rich regions in the eutectic mixture act as cathodic regions, whereas the IMCs distributed in the matrix and in the eutectic region act as anodic areas, thus evidencing a galvanic couple. Studies conducted with Zn-Mg alloys having smaller Mg content showed that the decrease in the cathodic area-Ac/anodic area-Aa ratio results in lower corrosion resistance<sup>7,40,41</sup>. For the alloy examined in the present study, the sample P\_70mm, with a coarser microstructure, has Aa (IMCs) larger than Ac (eutectic Zn); and, therefore, a greater corrosion rate as compared to that of sample P\_10mm. In this sense, SEM images for both samples were converted into binary images (using the ImageJ® software), in which the black areas are active (Mg-rich region) and white areas are nobler regions (rich in Zn), as shown in Figure 12. Sample P\_10mm [Figure 12(a)] (lower levels of Mg) have Ac/Aa equal to 1.6, while sample P\_70mm [Figure 12(b)] has Ac/Aa equal to 1.0. This lower Ac/Aa ratio has a negative effect on the electrochemical parameters leading the sample of coarser microstructure (P\_70mm) to more intense corrosion degradation, which can be used for stent production.

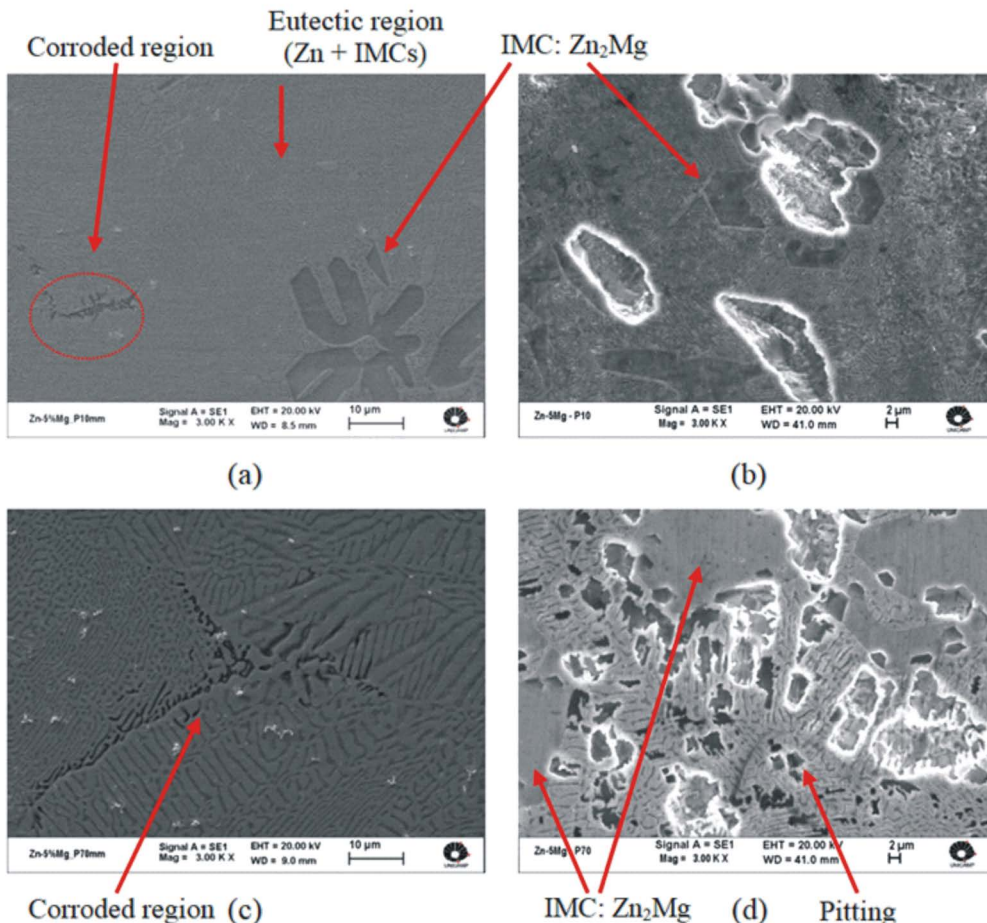


**Figure 11.** SEM images after corrosion tests: (a) and (b) sample P\_10mm and (c) and (d) sample P\_70mm.

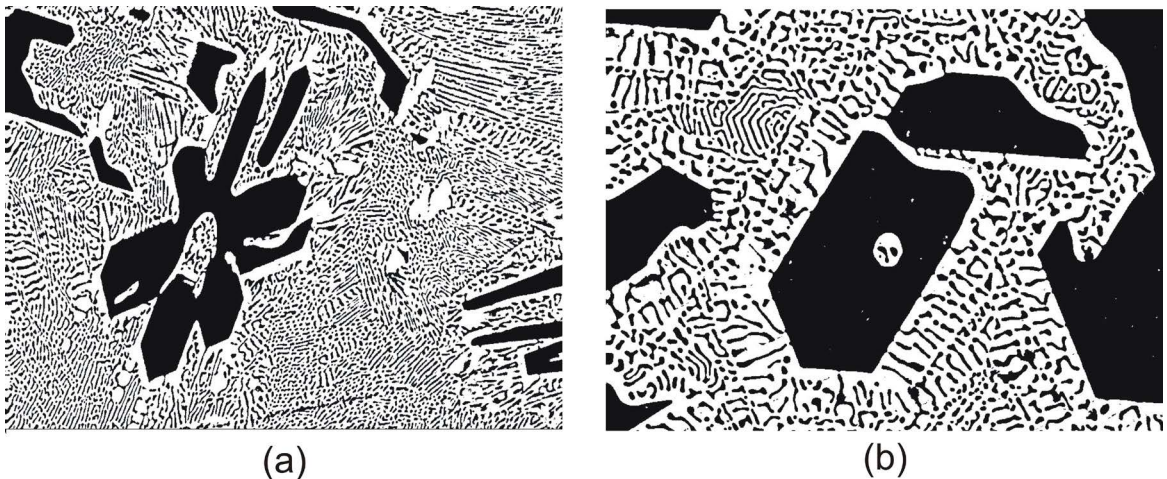


Figure 12. Binary images (using the ImageJ® software): (a) sample P\_10mm IMCs = 39% and (b) sample P\_70mm IMCs = 50%.

## 4. Conclusions

The findings of this study were:

A normal Mg macrosegregation profile, that is, an increasing Mg profile (from about 3.5 up to 6.25 wt.%Mg) from the bottom to the top of the vertical DS Zn-5.0wt.%Mg alloy casting was observed to occur, which was caused by the rejection of Mg at the solidification front. Since Mg has a lower density as compared to that of Zn, the liquid enriched by Mg has progressively moved upwards producing the macrosegregation profile.

The Zn-5.0wt.%Mg alloy casting showed a macrostructure typified only by equiaxed grains and a eutectic microstructure with two types of competitive eutectic mixtures (Zn+Mg<sub>2</sub>Zn<sub>11</sub> and Zn+MgZn<sub>2</sub>) and idiomorphic crystals of MgZn<sub>2</sub>, which were simultaneously observed along the entire range of analyzed solidification cooling rates.

An experimental power function growth law is proposed, relating the eutectic interlamellar spacing ( $\lambda_{cut}$ ) to the cooling rate ( $\dot{T}$ ). This correlation agrees with the Jackson-Hunt classical equation for the growth of lamellar eutectics.

The experimental Vickers microhardness profile was shown to decrease from bottom to top of the DS casting, that is, with the decrease in  $\dot{T}$  and consequent increase in  $\lambda_{cut}$  associated with the increase in the Mg content due to macrosegregation.

Analyses of experimental and calculated results of EIS and potentiodynamic polarization curves showed that a Zn-5.0wt.%Mg alloy sample with a more refined microstructure has a better resistance to corrosion.

## 5. Acknowledgments

The authors thank the financial support provided by: São Paulo Research Foundation – FAPESP (Grants: 2012/08494-0, 2013/15478-3, 2013/25452-1, 2013/23396-7, 2014/50502-5),

National Council for Scientific and Technological Development – CNPq (155863/2013-4, Project i-link0944, 166912/2017-4), Coordenação de Aperfeiçoamento de Pessoal de Nível Superior, Brazil - Capes (Funding Code 001), CNPEM and LNNano for the use of the XRD equipment. The authors thank Espaço da Escrita - Pró Reitoria de Pesquisa - UNICAMP- for the language services provided.

## 6. References

1. Yao C, Wang Z, Tay SL, Zhu T, Gao W. Effects of Mg on microstructure and corrosion properties of Zn-Mg alloy. *Journal of Alloys and Compounds*. 2014;602:101-107.
2. Chen D, He Y, Tao H, Zhang Y, Jiang Y, Zhang X, et al. Biocompatibility of magnesium-zinc alloy in biodegradable orthopedic implants. *International Journal of Molecular Medicine*. 2011;28(3):343-348.
3. Wang X, Lu HM, Li XL, Li L, Zheng YF. Effect of Cooling Rate and Composition on Microstructures and Properties of Zn-Mg Alloys. *Transactions of Nonferrous Metals Society of China*. 2007;17:s122-s125.
4. Vida TA, Freitas ES, Brito C, Cheung N, Arenas MA, Conde A, et al. Thermal Parameters and Microstructural Development in Directionally Solidified Zn-rich Zn-Mg Alloys. *Metallurgical and Materials Transactions A*. 2016;47(6):3052-3064.
5. Liu HY, Jones H. Solidification microstructure selection and characteristics in the zinc-based Zn-Mg system. *Acta Metallurgica et Materialia*. 1992;40(2):229-239.
6. Vida TA, Conde A, Freitas ES, Arenas MA, Cheung N, Brito C, et al. Directionally solidified dilute Zn-Mg alloys: Correlation between microstructure and corrosion properties. *Journal of Alloys and Compounds*. 2017;723:536-547.
7. Vida TA, Freitas ES, Cheung N, Garcia A, Osório WR. Electrochemical Corrosion Behavior of As-cast Zn-rich Zn-Mg Alloys in a 0.06 M NaCl Solution. *International Journal of Electrochemical Science*. 2017;12:5264-5283.

8. Krieg R, Vimalanandan A, Rohwerder M. Corrosion of Zinc and Zn-Mg Alloys with Varying Microstructures and Magnesium Contents. *Journal of The Electrochemical Society*. 2014;161(3):C156-C161.
9. Yao C, Wang Z, Tay SL, Zhu T, Gao W. Effects of Mg on microstructure and corrosion properties of Zn–Mg alloy. *Journal of Alloys and Compounds*. 2014;602:101-107.
10. Kelly RG, Scully JR, Shoemsmith D, Buchheit RG. *Electrochemical Techniques in Corrosion Science and Engineering*. New York: Marcel Dekker; 2002.
11. Prosek T, Nazarov A, Bexell U, Thierry D, Serak J. Corrosion mechanism of model zinc–magnesium alloys in atmospheric conditions. *Corrosion Science*. 2008;50(8):2216-2231.
12. Byun JM, Yu JM, Kim DK, Kim TY, Jung WS, Kim YD. Corrosion behavior of  $Mg_2Zn_{11}$  and  $MgZn_2$  single phases. *Journal of the Korean Institute of Metals and Materials*. 2013;51(6):413-419.
13. Mostaed E, Sikora-Jasinska M, Drelich JW, Vedani M. Zinc-based alloys for degradable vascular stent applications. *Acta Biomaterialia*. 2018;71:1-23.
14. Vojtěch D, Kubásek J, Šerák J, Novák P. Mechanical and corrosion properties of newly developed biodegradable Zn-based alloys for bone fixation. *Acta Biomaterialia*. 2011;7(9):3515-3522.
15. Pinto MA, Cheung N, Ierardi MCF, Garcia A. Microstructural and hardness investigation of an aluminum–copper alloy processed by laser surface melting. *Materials Characterization*. 2003;50(2-3):249-253.
16. Garcia LR, Osório WR, Peixoto LC, Garcia A. Wetting Behavior and Mechanical Properties of Sn-Zn and Sn-Pb Solder Alloys. *Journal of Electronic Materials*. 2009;38(11):2405-2414.
17. Goulart PR, Spinelli JE, Cheung N, Garcia A. The effects of cell spacing and distribution of intermetallic fibers on the mechanical properties of hypoeutectic Al-Fe alloys. *Materials Chemistry and Physics*. 2010;119(1-2):272-278.
18. Garcia LR, Osório WR, Peixoto LC, Garcia A. Mechanical properties of Sn–Zn lead-free solder alloys based on the microstructure array. *Materials Characterization*. 2010;61(2):212-220.
19. Osório WR, Freitas ES, Garcia A. Electrochemical Impedance Spectroscopy and Potentiodynamic Polarization Studies Affected by the Microstructure Array of a Monotectic Al-Pb Alloy in a NaCl Solution. *Corrosion*. 2014;70(10):1031-1042.
20. Bertelli F, Brito C, Ferreira IL, Reinhart G, Nguyen-Thi H, Manginck-Noël N, et al. Cooling thermal parameters, microstructure, segregation and hardness in directionally solidified Al–Sn(Si; Cu) alloys. *Materials & Design*. 2015;72:31-42.
21. Silva BL, Cheung N, Garcia A, Spinelli JE. Sn–0.7 wt% Cu–(xNi) alloys: Microstructure–mechanical properties correlations with solder/substrate interfacial heat transfer coefficient. *Journal of Alloys and Compounds*. 2015;632:274-285.
22. Santos WLR, Brito C, Quaresma JMV, Spinelli JE, Garcia A. Plate-like cell growth during directional solidification of a Zn–20wt% Sn high-temperature lead-free solder alloy. *Materials Science and Engineering: B*. 2014;182:29-36.
23. Lasia A. *Electrochemical Impedance Spectroscopy and its Applications*. New York: Springer; 2014.
24. Yao C, Wang Z, Tay SL, Gao W. Effects of Mg on morphologies and properties of hot dipped Zn–Mg coatings. *Surface and Coatings Technology*. 2014;260:39-45.
25. Jackson KA, Hunt JD. Lamellar and Rod Eutectic Growth. *Transactions of the Metallurgical Society of AIME*. 1966;236:1129-1142.
26. Xu Z, Li Z, Peng L, Yan J. Ultra-rapid transient liquid phase bonding of Mg alloys within 1s in air by ultrasonic assistance. *Materials & Design*. 2019;161:72-79.
27. Jia H, Feng X, Yang Y. Effect of crystal orientation on corrosion behavior of directionally solidified Mg–4 wt% Zn alloy. *Journal of Materials Science & Technology*. 2018;34(7):1229-1235.
28. Savova-Stoynov B, Stoynov ZB. Analysis of the inductance influence on the measured electrochemical impedance. *Journal of Applied Electrochemistry*. 1987;17(6):1150-1158.
29. James M, Kumar S, Narayanan TSNS. Corrosion behavior of commercially pure Mg and ZM21 Mg alloy in Ringer’s solution–Long term evaluation by EIS. *Corrosion Science*. 2011;53(2):645-654.
30. Zhang J, Dai C, Wen Z, Wei J. Study on the Effect of the Coating Thickness on Corrosion Behavior of AZ91D Magnesium Alloy in m-SBF. *International Journal of Electrochemical Science*. 2015;10:6002-6013.
31. Yang Q, Xu J, Chen L, Gong Y, Sun X, Chen C. The Effects of  $NaHCO_3$  on the Voltage Delay of Mg Cell with AZ31B Magnesium Alloy in  $Mg(ClO_4)_2$  Electrolytic Solution. *Journal of The Electrochemical Society*. 2017;164(4):A630-A637.
32. Osório WR, Peixoto LC, Canté MV, Garcia A. Electrochemical corrosion characterization of Al–Ni alloys in a dilute sodium chloride solution. *Electrochimica Acta*. 2010;55(13):4078-4085.
33. Peixoto LC, Bortolozzo AD, Garcia A, Osório WR. Performance of New Pb-Bi Alloys for Pb-Acid Battery Applications: EIS and Polarization Study. *Journal of Materials Engineering and Performance*. 2016;25(6):2211-2221.
34. Osório WR, Moutinho DJ, Peixoto LC, Ferreira IL, Garcia A. Macrosegregation and microstructure dendritic array affecting the electrochemical behaviour of ternary Al–Cu–Si alloys. *Electrochimica Acta*. 2011;56(24):8412-8421.
35. Osório WR, Peixoto LC, Garcia LR, Garcia A. Corrosion behavior of hypoeutectic Al-Cu alloys in  $H_2SO_4$  and NaCl solutions. *Acta Metallurgica Sinica (English Letters)*. 2009;22(4):241-246.
36. Zhao M, Wu S, An P, Luo J. Study on the deterioration process of a chromium-free conversion coating on AZ91D magnesium alloy in NaCl solution. *Applied Surface Science*. 2006;253(2):468-475.
37. Pinto GM, Nayak J, Shetty AN. Corrosion behaviour of 6061 Al-15vol. Pct. SiC Composite and its Base Alloy in a Mixture of 1:1 Hydrochloric and Sulphuric Acid Medium. *International Journal of Electrochemical Science*. 2009;4:1452-1468.
38. Jingling MA, Jiuba W, Gengxin LI, Chunhua XV. The corrosion behaviour of Al–Zn–In–Mg–Ti alloy in NaCl solution. *Corrosion Science*. 2010;52(2):534-539.
39. Martin H, Carro P, Hernández Creus A, Morales J, Fernández G, Esparza P, et al. Interplay of Surface Diffusion and Surface Tension in the Evolution of Solid/Liquid Interfaces. Dealloying of  $\beta$ -Brass in Aqueous Sodium Chloride. *The Journal of Physical Chemistry B*. 2000;104(34):8229-8237.

40. Osório WR, Peixoto LC, Garcia A. Electrochemical and Mechanical Behavior of Lead-Silver and Lead-Bismuth Casting Alloys for Lead-Acid Battery Components. *Metallurgical and Materials Transactions A*. 2015;46(9):4255-4267.
41. Verissimo NC, Freitas ES, Cheung N, Garcia A, Osório WR. The effects of Zn segregation and microstructure length scale on the corrosion behavior of a directionally solidified Mg-25 wt.%Zn alloy. *Journal of Alloys and Compounds*. 2017;723:649-660.